Large-area phase-contrast X-ray imaging using a two-crystal X-ray interferometer

Akio Yoneyama,[a]* Atsushi Momose,[b] Ichiro Koyama,[b] Eiichi Seya,[c] Tohoru Takeda,[d] Yuji Itai,[d] Keiichi Hirano[e] and Kazuyuki Hyodo[e]

[a]Advanced Research Laboratory, Hitachi Ltd, Hatoyama, Saitama 350-0395, Japan, [b]Department of Applied Physics, The University of Tokyo, 7-3-1 Hongo, Bunkyo-ku, Tokyo 113-8656, Japan, [c]Central Research Laboratory, Hitachi Ltd, Kokubunji, Tokyo 185-8601, Japan, [d]Institute of Clinical Medicine, University of Tsukuba, Tsukuba, Ibaraki 350-8575, Japan, and [e]Institute of Materials Science, High Energy Accelerator Research Organization, Tsukuba, Ibaraki 305-0801, Japan. E-mail: a-yoneya@harl.hitachi.co.jp

Large-area (25 × 20 mm) phase-contrast X-ray imaging was attained by using a skew-symmetric two-crystal X-ray interferometer. The sub-nrad angular control required to operate the X-ray interferometer was achieved with a sleeve bearing and a feedback-positioning system. As a demonstration, measurements of a phase map of a rat's liver and a phase-contrast tomographic three-dimensional image of a piece of a rabbit's liver were performed at the Photon Factory using 0.07 nm synchrotron radiation X-rays.

Keywords: phase-contrast; X-ray imaging; two-crystal X-ray interferometer; phase-contrast computed tomography; cancer.

1. Introduction

Absorption-contrast X-ray imaging is widely used for the non-destructive observation of the inner structures of samples. However, light elements have a small absorption cross section in the hard-X-ray energy region, so the observation of samples that consist mainly of light elements, such as biological soft tissue, is difficult. On the other hand, phase-contrast X-ray imaging enables the observation of such light samples without a contrast agent, because the phase-shift cross sections of light elements are much larger than their absorption cross sections.

For phase-contrast X-ray imaging, the X-ray interferometer (Bonse & Hart, 1965) is a powerful tool. By using monolithic triple Laue-case (LLL) X-ray interferometers (Fig. 1*a*), structures in a rat cerebellum have been revealed (Momose & Fukuda, 1995). Three-dimensional observation of various forms of biological soft tissue by phase-contrast computed tomography (CT) (Momose, 1995) has also been demonstrated (Momose *et al.*, 1996; Beckmann *et al.*, 1997; Takeda *et al.*, 2000). The advantage of the monolithic LLL X-ray interferometer is that stability is easily achieved for the instrument's various components, and this makes its operation comparatively easy. However, the field of view is limited by the size of the silicon ingot from which the interferometer has been cut out. In addition, in the imaging of live objects, a deformation of the crystal wafers caused by the sample's heat is unavoidable. This causes fluctuations in the interference pattern.

In order to overcome this limitation and thermal disturbance, we have been studying a skew-symmetric two-crystal X-ray interferometer (STXI) (Fig. 1*b*). The configuration of this device was initially designed to lengthen the path of the interfering beam (Becker & Bonse, 1974). Forming an X-ray interferometer in this configuration doubles the field of view for a silicon ingot of a given size. Aligning the blocks of this device at a moderate distance from each other provides a way to minimize the thermal effect. On the other hand, the difference between the lengths of the optical paths for the object beam and reference beam has to be kept constant and of the same order as the X-ray wavelength for the system to operate.

For phase-contrast X-ray imaging with practical times of measurement, the use of synchrotron radiation is indispensable. However, we were unsure whether or not it would be possible for an STXI to function at a synchrotron radiation facility. As a first stage, therefore, we fabricated a small STXI and performed its operation with synchrotron radiation at the Photon Factory (Momose *et al.*, 1997). As a second stage, we developed an STXI imaging system with a 25 × 15 mm field of view and a feedback system to stabilize the optical system, and demonstrated the system's successful operation and the observation of a phase map for a biological sample (Yoneyama *et al.*, 1999).

For the next stage, we developed a 30 × 30 mm field-of-view STXI imaging system for the phase-contrast CT of large samples and for *in vivo* phase-contrast observations. In this article, we will report on the new imaging system and our successful use of it to observe the interference pattern, phase map and three-dimensional image of biological samples.

2. Skew-symmetric two-crystal X-ray interferometer

The STXI consists of two independent crystal blocks that carry two crystal wafers, as shown in Fig. 1(*b*). Incident X-rays are separated into two beams by the splitter *S* of the first block. These beams are reflected by the mirrors *M*1 and *M*2, respectively, and are combined by the analyzer *A* to form two post-analyzer interference beams. The advantage of the configuration of the STXI is that the parallel linear displacement between the crystal blocks does not affect the lengths of the optical paths, so only two rotations (θ and φ) need to be controlled.

The angular deviation $\Delta\theta$ changes the position of the lattice planes of *M*2 and *A* relative to each other and causes a phase difference $\Delta\Phi$

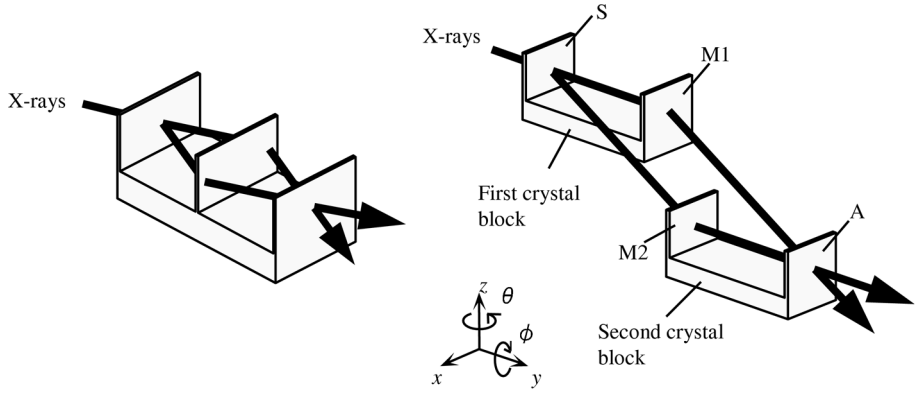

Figure 1
(*a*) A monolithic LLL interferometer and (*b*) a skew-symmetric two-crystal interferometer; only two rotations (θ and φ) need to be controlled.

between the object beam and the reference beam. The relation between $\Delta\theta$ and $\Delta\Phi$ is given by

$$\Delta\Phi = 2\pi(x + t)\Delta\theta/d, \quad (1)$$

where x, t and d are the path length of the beam between the wafers on each of the blocks, the thickness of the wafers and the Bragg-plane spacing, respectively (Becker & Bonse, 1974). For the blocks that we fabricated [where $x = 80$ mm, $t = 1$ mm and $d = 0.192$ nm (Si 220 diffraction)], $\Delta\theta = 2.4$ nrad corresponds to a phase difference of 2π. If the value of $\Delta\Phi$ exceeds 2π during the exposure for the recording of an interference image, the interference fringes are smeared out. Therefore, the θ rotation should be stabilized with an accuracy of sub-nrad order.

When the φ rotation is detuned, a fringe pattern that corresponds to a rotation Moiré pattern appears (Becker & Bonse, 1974). The spacing Λ of the Moiré fringes is given by

$$\Lambda = \lambda L/(2x\Delta\varphi \sin\theta_B), \quad (2)$$

where λ, L and θ_B are the wavelength of the X-rays, the distance from the X-ray source to the image detector and the Bragg diffraction angle, respectively. The φ rotation should be tuned so that Λ is much larger than the spatial resolution of the image detector. For our typical experimental conditions, $\lambda = 0.07$ nm (17.7 keV), $L = 20$ m and $\theta_B = 10.5°$, an accuracy of better than 10 µrad is required to achieve $\Lambda \geq 5$ mm.

3. Apparatus

3.1. Mechanical positioning system

The mechanical positioning system for STXI requires tables that are rotatable in θ and φ, as explained above. In addition, a further rotating table is needed to set the X-ray interferometer in the Bragg condition against the incident X-rays. These rotating tables must be highly rigid to minimize the propagation of the floor's vibrations into the crystal blocks, which would cause fluctuations in the phase difference $\Delta\Phi$.

Fig. 2 shows the new system we have developed to satisfy these conditions. One of the crystal blocks was mounted on an *S*2 table for the θ rotation, while the other was mounted on a tilt table for the φ rotation. The *S*1 table that carried the *S*2 table and the tilt table was used to adjust the angle of incidence of the X-rays on the *S* wafer of the first crystal block. To improve the rigidity of the tables and avoid the deformation of the tables by gravitation, the beam paths were formed in the horizontal plane, and the *S*1 and *S*2 tables thus rotate around vertical axes.

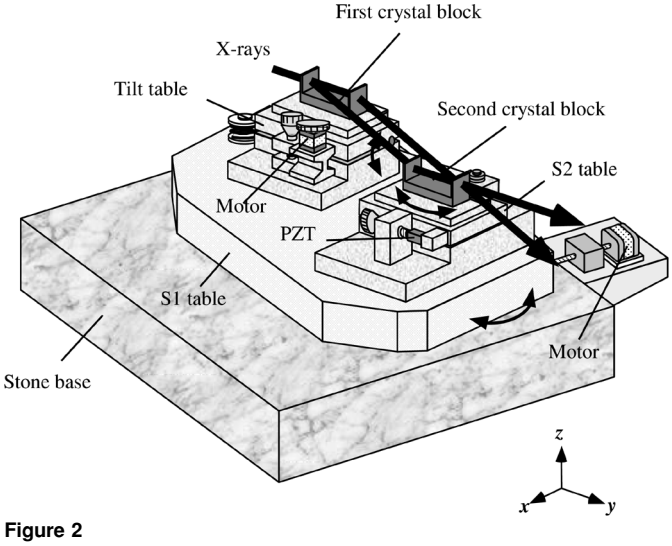

Figure 2
A schematic view of the positioning system for the skew-symmetric two-crystal X-ray interferometer. The *S*2 and tilt tables control the θ and φ rotation of the crystal blocks relative to each other. The *S*1 table, which carries the *S*2 and tilt tables, controls the angle of incidence of the X-rays.

The required accuracy of sub-nrad order for the *S*2 table was achieved by a fine-adjustment mechanism, consisting of a sleeve bearing and a feedback-positioning system (described later). The fine-adjustment mechanism consisted of a laminated piezoelectric actuator (PZT) that expanded by 15 µm at 100 V relative to its thickness at 0 V and a voltage source that supplied 0–100 V at a resolution of 0.1 mV. The resulting minimum angular step was 0.07 nrad, which corresponds to a phase difference $\Delta\Phi = \pi/17$. The sleeve bearing was employed to reduce the mechanical vibration of the table by increasing the rigidity of the table; the *S*2 table slides on the *S*1 table with a slippery sheet of polyterafluoroethylene (PTFE) pasted on the bottom of the *S*2 table. The size of the *S*2 table was 180×70 mm, which was large enough for the mounting of one crystal block of an STXI that is able to generate a 30×30 mm field of view.

The required accuracy for the tilt table was easily achieved with an adjustment mechanism driven by a stepping motor. The minimum angular step of the tilt table was 5 µrad, which achieves $\Lambda = 10$ mm. The tilt table was of the same size as the *S*2 table. The required accuracy for the *S*1 table was also easily achieved with an adjustment mechanism driven by a stepping motor. The minimum angular step of the *S*1 table was 0.01 µrad, which was sufficient to adjust the angle of incidence of the X-rays on the *S* wafer to the Bragg diffraction angle. A sleeve bearing was also employed in order to reduce the mechanical vibration of the table by increasing the rigidity of the table.

The airflow around the interferometer causes thermal non-uniformity in the crystal wafers and deforms them. In addition, any sound vibrations around the interferometer make the rotating tables vibrate. As a result, these disturbances create a fluctuation of $\Delta\Phi$ in the phase difference. To avoid this fluctuation, outer and inner hoods were employed. The outer hood covered the whole positioning system, and individual inner hoods covered the *S*1 table and the tilt table. Each hood has holes in the direction of the X-ray beam's path, and polyamide films were placed over these holes.

3.2. Feedback-positioning system

The drift in θ rotation causes an undesirable phase difference $\Delta\Phi$, which is described by (1). However, the fine-adjustment mechanism of the *S*2 table was unable to cope with this drift. The feedback-positioning system of the *S*2 table (Yoneyama *et al.*, 1999) was thus employed to suppress this drift. In this system, the voltage applied to the piezoelectric actuator of the *S*2 table is controlled so that the intensity of a small section of the interference beam, which varies with the value of $\Delta\theta$, follows the target intensity. The target intensity was changed according to the decrease in the electron-beam current in the storage ring. Because the measurement time required for phase-contrast CT is more than a few hours, the decrease in the intensity of the beam of incident X-rays caused by the decrease in the beam current is non-negligible.

The drift of the *S*1 table was also a crucial factor to control for long-term measurements. Therefore, a feedback-positioning system was also applied to the *S*1 table. This system controlled the *S*1 table to keep the intensity of the beam as it passed through the two wafers of the first crystal block at the target intensity.

4. Results

4.1. Experimental set-up

The experiments were performed at BL-14C1 of the Photon Factory, Tsukuba, Japan, using synchrotron radiation from a vertical wiggler. The vertical wiggler emits a beam that fans out in the vertical direction, which can be expanded by applying asymmetrical diffraction in the horizontal direction. As was mentioned above, the beam paths of the X-ray interferometer are formed in the horizontal plane, and using this source therefore minimizes the loss of X-ray intensity as the beam passes through the X-ray interferometer.

Fig. 3 shows the experimental set-up at BL-14C1. The X-ray beam from the vertical wiggler was monochromated by an Si(220) double-crystal monochromator (not shown) and introduced into the experimental hatch. Next, the beam was diffracted by an asymmetric crystal whose surface was inclined by 9.5° from the (110) plane in order to expand the size of the beam to 34 mm (width) × 30 mm (height).

In the test of this system, we used the crystal blocks that we had fabricated for a previous set of experiments (Yoneyama *et al.*, 1999), and the field of view was thus 25 mm wide and 20 mm high. One of the two post-analyzer interference beams was detected by a 4 k × 4 k pixel CCD-based imaging detector (Momose *et al.*, 2001) or by an X-ray-sensing pickup tube (Suzuki *et al.*, 1989). The other interference beam was narrowed by the four-quadrant slit and detected by the scintillation counter of the feedback-positioning system for the *S*2 table. The intensity of the beam that passed through the two wafers of the first crystal block was detected by a PIN photodiode of the feedback-positioning system for the *S*1 table.

4.2. Interference pattern

With the alignment process described in the previous paper (Yoneyama *et al.*, 1999), an interference pattern was obtained using 0.07 nm X-rays, and this is shown in Fig. 4. This image was detected with a 10 s exposure by the CCD-based imaging detector. The image was of a region 25 mm wide and 20 mm high, and the best visibility was 45%, which is high enough for phase-contrast X-ray imaging. No object was placed in the path of the interference beams, so the fringes seen in the figure were caused by unevenness of the lattice spacing and/or deformation of the crystal blocks.

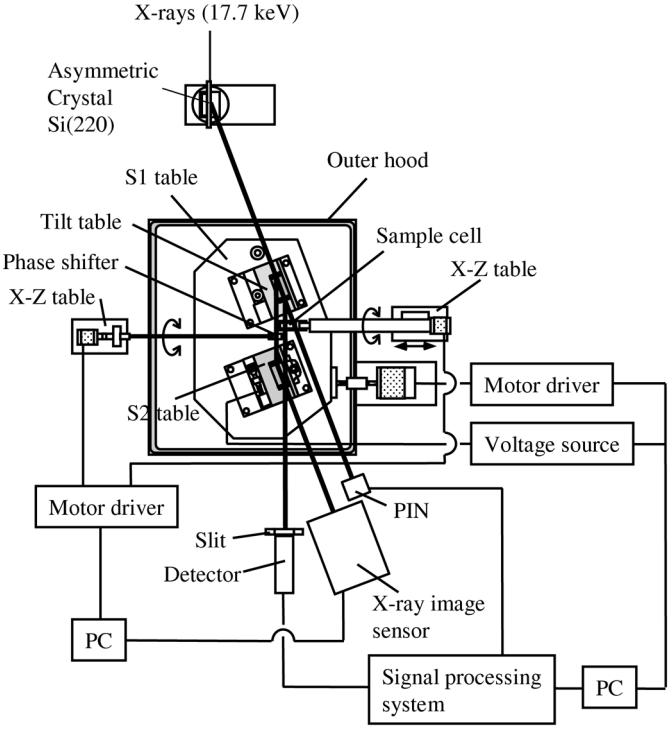

Figure 3
Experimental set-up at BL-14C1 at the Photon Factory.

4.3. Testing the performance of the feedback system for the *S*2 table

Fig. 5 shows a chart of X-ray intensity over time as monitored for a small section of the interference pattern, along with the voltage applied to the PZT for the *S*2 table. A 100 × 100 μm section was monitored. This is smaller than the scale of the spacing of the interference fringes. The sampling clock of the system was 1 Hz, and the time constant of the feedback was 3 s.

While the feedback system was off, the intensity oscillated because of the drift in θ. After the feedback control was applied, the intensity was kept at the target value. The slow decrease in the intensity indicates the change in the target intensity with the decay of the beam

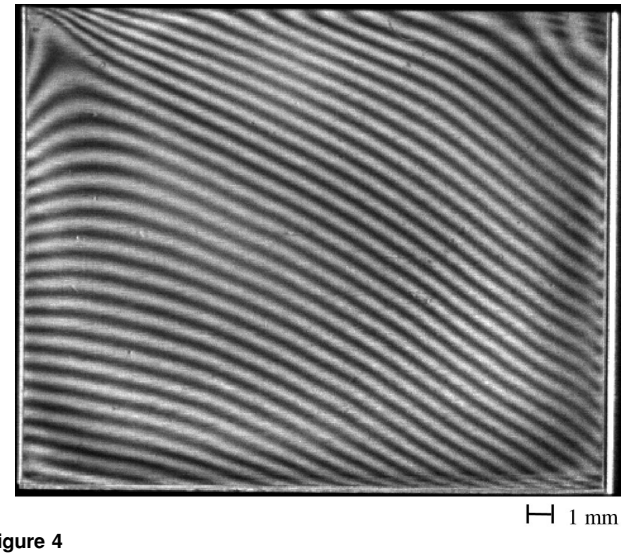

Figure 4
A 25 × 20 mm interference pattern obtained with 17.7 keV X-rays. The fringe visibility was 45%, which was sufficiently high for imaging. The fringes were caused by the unevenness of the lattice spacing of the crystal and/or deformation of the crystal blocks.

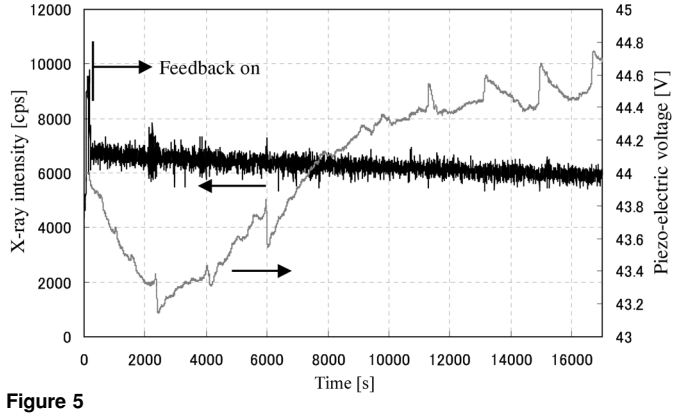

Figure 5
Chart over time of the intensity of a small section of the post-interference X-rays and of the voltage applied to the piezoelectric actuator of the *S*2 table. The voltage was controlled to keep the intensity at the target intensity by taking account of the decrease in the beam current in the storage ring.

current in the storage ring. The standard deviation of the difference between the monitored intensity and the target intensity for the oscillation amplitude of 5000 counts s^{-1} was about 350 counts s^{-1}. Taking account of the level of quantum noise ($6000^{1/2} = 77$), this result suggests that the *S*2 table was stabilized nominally within 0.1 nrad, which corresponds to a phase difference of $\pi/16$.

4.4. Phase map

This apparatus was then applied to measure a phase map (spatial distribution of the phase shift caused by the sample) by using the fringe-scanning method (Bruning *et al.*, 1974). The sample and a plastic plate as a phase shifter were placed in the object and reference beam paths as shown in Fig. 3. Each is individually supported by rods connected to the horizontal and vertical linear tables. These tables were located outside the outer hood in order to prevent disturbance of the interference by the motor's vibration. The plastic plate was rotated by the stepping motor to change the phase difference between the object beam and the reference beam. The sample was placed in a cell filled with water in order to avoid the generation of overly fine interference fringes by variations in the thickness of the sample (Momose, 1995).

To obtain the phase map of a sample, we began by obtaining a background phase map Φ_{bk}, *i.e.* a map with no sample in the paths of the interference beam. Next, we placed a sample in the beam path and obtained a phase map of the form $\Phi_{bk} + \Phi$. Finally, the phase map Φ was obtained from $\Phi_{bk} + \Phi$ by subtracting the background phase map Φ_{bk}.

Fig. 6 shows a phase map obtained for a rat's liver by a five-step fringe scan. Each of the five interference patterns was detected by the CCD-based imaging detector with a 10 s exposure. The image was of a region 17 mm wide and 15 mm high. The difference in phase shift between the water in the blood vessel and structural tissue of the liver made blood vessels with a diameter of about 50 μm visible as regions of gray contrast.

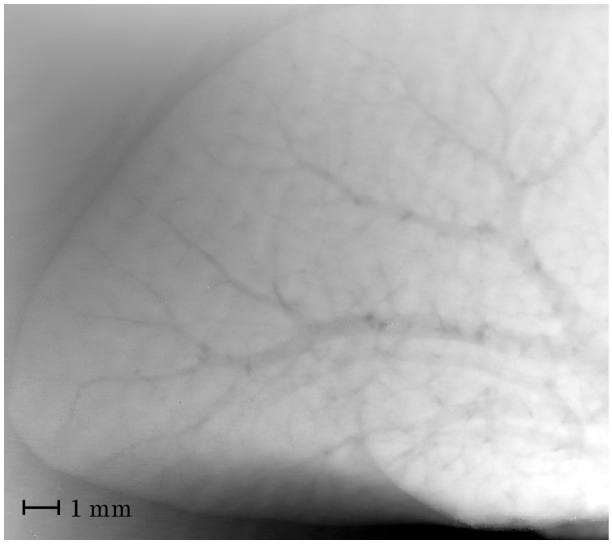

Figure 6
A 17 × 15 mm phase map obtained for a rat's liver by using the fringe-scanning method with five steps. Blood vessels with a diameter of about 50 μm were visible in the liver specimen.

4.5. Phase-contrast CT

Phase-contrast CT with this apparatus was also demonstrated. The phase maps of each projection for use in CT reconstruction were obtained with a five-step fringe scan. The sample was rotated through 180° in 0.72° steps (250 projections) in a cell filled with water. A filtered back-projection method with a Shepp–Logan filter was used to reconstruct the phase-contrast tomograms.

Fig. 7 shows a three-dimensional image of a columnar piece of the liver of a rabbit with VX2 cancer. Each interference pattern was detected by the X-ray-sensing pickup tube with a 12 s exposure. The diameter of the sample was about 10 mm and its height was 5 mm. The voxel size was 18 × 18 × 12 μm. The gray levels for the cancer tissue were lower than those for the normal tissue, and some fine structures were visible. Moreover, blood vessels with a diameter of about 30 μm in the normal tissue appeared as regions of gray contrast. This result is similar to one that was obtained previously with a monolithic LLL X-ray interferometer (Momose *et al.*, 1996).

5. Conclusion

A large-area phase-contrast X-ray imaging system, in which a two-crystal X-ray interferometer is applied, was developed and successfully operated. A 25 × 20 mm interference pattern with a best visibility of 45% was obtained. The phase difference caused by the drift in relative rotational positions of the separate crystal blocks was controlled to a deviation within 0.1 nrad for 4.5 h by using feedback systems. As a demonstration, a phase map of a rat's liver and a three-dimensional image of a columnar piece of a rabbit's liver were observed. The results prove that this system is useful for the large-area phase-contrast X-ray imaging of various samples.

In order to apply this imaging technique to *in vivo* observation, shortening of the period of measurement to within the order of a second will be necessary. A way to fulfil this requirement is to use the Fourier-transform method (Takeda *et al.*, 1982), which requires a single interference image to obtain a phase map. As our next step, *in vivo* phase-contrast observation with this method is in progress.

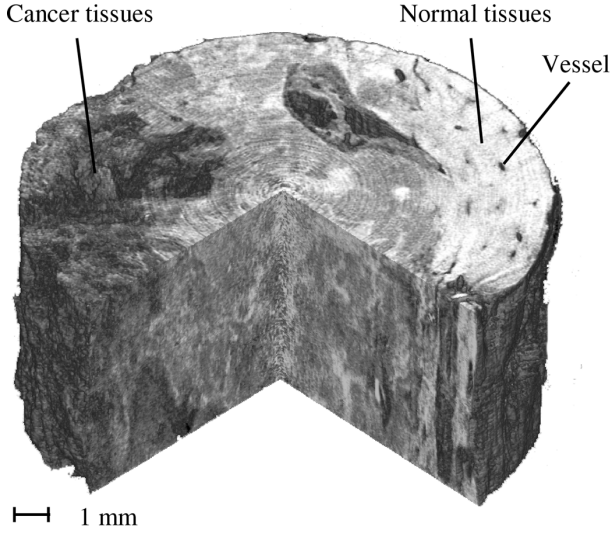

Figure 7
A three-dimensional image of a columnar piece of liver from a rabbit with VX2 cancer. The diameter of the sample was 10 mm, and its height was 5 mm. The gray levels for cancer tissues were lower than those for normal tissues, and some fine structures were visible.

This study was carried out with the assistance of the Special Coordination Fund of the Ministry of Education, Culture, Sports, Science and Technology of the Japanese Government. The experiments were performed under Proposal No. 99S2-002, approved by the High Energy Accelerator Research Organization.

References

Becker, P. & Bonse, U. (1974). *J. Appl. Cryst.* **7**, 593–598.
Beckmann, F., Bonse, U., Busch, F. & Gunnewig, O. (1997). *J. Comput. Assist. Tomogr.* **21**, 539–553.
Bonse, U. & Hart, M. (1965). *Appl. Phys. Lett.* **6**, 155–156.
Bruning, J. H., Herriott, D. R., Gallagher, J. E., Rosenfeld, D. P., White, A. D. & Brangaccio, D. J. (1974). *Appl. Opt.* **13**, 2693–2703.
Momose, A. (1995). *Nucl. Instrum. Methods*, A**352**, 622–628.
Momose, A. & Fukuda, J. (1995). *Med. Phys.* **22**, 375–380.
Momose, A., Takeda, T., Itai, Y. & Hirano, K. (1996). *Nature Med.* **2**, 473–475.
Momose, A., Takeda, T., Yoneyama, A., Koyama, I. & Itai, Y. (2001). *Nucl. Instrum. Methods Phys. Res.* A**467**/**468**, 917–920.
Momose, A., Yoneyama, A. & Hirano, K. (1997). *J. Synchrotron Rad.* **4**, 311–312.
Suzuki, Y., Hayakawa, K., Usami, K., Hirano, T., Endoh, T. & Okamura, Y. (1989). *Rev. Sci. Instrum.* **60**, 2299–2302.
Takeda, M., Ina, H. & Kobayashi, S. (1982). *J. Opt. Soc. Am.* **72**, 156–160.
Takeda, T., Momose, A., Hirano, K., Haraoka, S., Watanabe, T. & Itai, Y. (2000). *Radiology*, **214**, 298–301.
Yoneyama, A., Momose, A., Seya, E., Hirano, K., Takeda, T. & Itai, Y. (1999). *Rev. Sci. Instrum.* **70**, 4582–4586.

 Received 11 March 2002 • Accepted 24 July 2002